

# Fabrication of bimetallic Cu–Zn adsorbents with high dispersion by using confined space for gas adsorptive separation

Yu-Chao Wang\*, Tian-Tian Li\*, Li Huang, Xiao-Qin Liu, Lin-Bing Sun (✉)

State Key Laboratory of Materials-Oriented Chemical Engineering, Jiangsu National Synergetic Innovation Center for Advanced Materials (SICAM), College of Chemical Engineering, Nanjing Tech University, Nanjing 211816, China

© Higher Education Press 2022

**Abstract** The number of active components and their dispersion degree are two key factors affecting the performance of adsorbents. Here, we report a simple but efficient strategy for dispersing active components by using a confined space, which is formed by mesoporous silica walls and templates in the as-prepared SBA-15 (AS). Such a confined space does not exist in the conventional support, calcined SBA-15, which does not contain a template. The Cu and Zn precursors were introduced to the confined space in the AS and were converted to CuO and ZnO during calcination, during which the template was also removed. The results show that up to  $5 \text{ mmol} \cdot \text{g}^{-1}$  of CuO and ZnO can be well dispersed; however, severe aggregation of both oxides takes place in the sample derived from the calcined SBA-15 with the same loading. Confined space in the AS and the strong interactions caused by the abundant hydroxyl groups are responsible for the dispersion of CuO and ZnO. The bimetallic materials were employed for the adsorptive separation of propene and propane. The samples prepared from the as-prepared SBA-15 showed superior performance to their counterparts from the calcined SBA-15 in terms of both adsorption capacity of propene and selectivity for propene/propane.

**Keywords** bimetallic adsorbents, confined space, mesoporous silica, propene/propane separation

## 1 Introduction

Adsorptive separation plays a critical role in the chemical

[1–5], pharmaceutical [6–8], energy [9–11] and environmental fields [12–16]. Compared to other separation methods, adsorption has unique advantages; for example, it requires little energy and does not involve the introduction of new substances. The key point of adsorptive separation is the development of highly efficient adsorbents [17–21]. Since the discovery of mesoporous materials [22–24], such materials have been used as ideal carriers of adsorbents due to their unique physicochemical properties [25–28]. Wu and Zhao [29] studied the adsorption capacity of various mesoporous materials. The results showed that mesoporous materials have high potential for applications in adsorption. These materials, such as MCM-41 and SBA-15, have large specific surface areas and high pore volumes [30–34], but they have few active centers, so they are often used for physical adsorption. Thus, the modification of mesoporous materials has always been a common research topic.

Various methods for modifying mesoporous materials have been used [35–37]. Yin et al. [38] loaded CuO on SBA-15 to adsorb thiophene. The results clearly showed that the adsorption performance was enhanced with metal loading. Shi et al. [39] introduced NiO into mesoporous materials, and the obtained materials exhibited excellent catalytic activity. With the continuous improvement of industrial requirements, more attention has been given to the development of bimetallic adsorbents. Wang et al. [40] prepared a Zn/Cu-BTC adsorbent for adsorption desulfurization. It was found that the introduction of Zn promoted the  $\pi$ -complexation adsorption of benzothiophene on Cu. Khan et al. [41] used the synergy between Cu and Ce in Cu–Ce/MIL-101 to improve the desulfurization performance. Dammaliki et al. [42] simultaneously introduced Ce and Fe nanoparticles in oxidized activated carbon. The results showed that the bimetallic adsorbent exhibited better adsorption performance than the Ce or Fe

Received May 1, 2022; accepted May 25, 2022

E-mail: lbsun@njtech.edu.cn

\* These authors contributed equally to this work.

adsorbent alone. These results indicate that bimetallic sites play an important role in adsorptive separation.

The activity of adsorbents is closely related to the dispersion degree of the active components. In general, as-prepared mesoporous silica is first calcined to remove the template so that open pores that allow the accommodation of precursors can be obtained. There is a confined space with a special microenvironment between the template and silica walls in this mesoporous silica, as reported by Sun and coworkers [43]. In addition, a large number of hydroxyl groups, which should be able to interact with the active component, are present in such materials [44]. However, reports concerning the fabrication of bimetallic adsorbents by exploring the confined spaces in unmodified silica are very scarce.

Here, we report a facile but efficient strategy that utilizes the confined space in as-prepared SBA-15 (AS) to fabricate bimetallic adsorbents (Fig. 1). Such a confined space is not present in calcined SBA-15 (CS), which no longer has a template. The Cu and Zn precursors were introduced to the confined space in the AS and were converted to CuO and ZnO during calcination, in which the template was removed simultaneously. Our results showed that the Cu–Zn bimetallic adsorbents derived from the AS had better-dispersed active components than their counterparts from CS, leading to better adsorptive separation performance for C<sub>3</sub>H<sub>6</sub> and C<sub>3</sub>H<sub>8</sub>.

## 2 Experimental

### 2.1 Synthesis of Cu- and Zn-containing adsorbents

The precursors Cu(NO<sub>3</sub>)<sub>2</sub>·3H<sub>2</sub>O and Zn(NO<sub>3</sub>)<sub>2</sub>·6H<sub>2</sub>O were introduced to AS by solid-state grinding. The support AS and the precursors were put into a mortar. The mixture was ground manually under ambient conditions for approximately 30 min. The obtained solid was calcined in flowing air (20 mL·min<sup>-1</sup>) with a heating

rate of 2 °C·min<sup>-1</sup> at 400 °C for 2 h. The obtained sample was denoted *x*Cu–*y*Zn–AS (*x* and *y* represent the amount of CuO and ZnO in mmol·g<sup>-1</sup>, respectively). For example, 68 mg of Cu(NO<sub>3</sub>)<sub>2</sub>·3H<sub>2</sub>O and 84 mg of Zn(NO<sub>3</sub>)<sub>2</sub>·6H<sub>2</sub>O were introduced to 200 mg of the AS, followed by calcination to obtain the sample 3Cu–3Zn–AS. For comparison, Cu(NO<sub>3</sub>)<sub>2</sub>·3H<sub>2</sub>O and Zn(NO<sub>3</sub>)<sub>2</sub>·6H<sub>2</sub>O were also introduced to the CS via the process described above to obtain *x*Cu–*y*Zn–CS (*x* and *y* represent the amount of CuO and ZnO in mmol·g<sup>-1</sup>, respectively).

### 2.2 Gas adsorption test

The adsorption isotherms of C<sub>3</sub>H<sub>6</sub> and C<sub>3</sub>H<sub>8</sub> were obtained on an ASAP 2020 automatic surface area and porosity analyzer manufactured by Micromeritics (USA). The measurement was conducted at 0 °C, with pressure ranging from 0 to 100 kPa. The samples were pretreated for 3 h at 150 °C prior to testing.

## 3 Results and discussion

### 3.1 Dispersion of bimetallic oxides in confined space

The low-angle X-ray diffraction (XRD) patterns of the samples are shown in Fig. 2. The carrier CS exhibits one strong diffraction peak with two weak peaks at 2θ values of 0.9°, 1.6° and 1.8°, which reflect two-dimensional hexagonal pore symmetry [45]. All samples are similar in appearance, revealing that the ordered mesostructure of SBA-15 was retained. In addition, the intensity of the diffraction line corresponding to the (100) crystal plane is lower in the Cu–Zn–CS samples than in Cu–Zn–AS, indicating that the formed CuO and ZnO blocked some of the pores, reducing the scattering difference. The *d*-spacings of Cu–Zn–AS samples also shift toward higher values compared to those of the CS samples. The

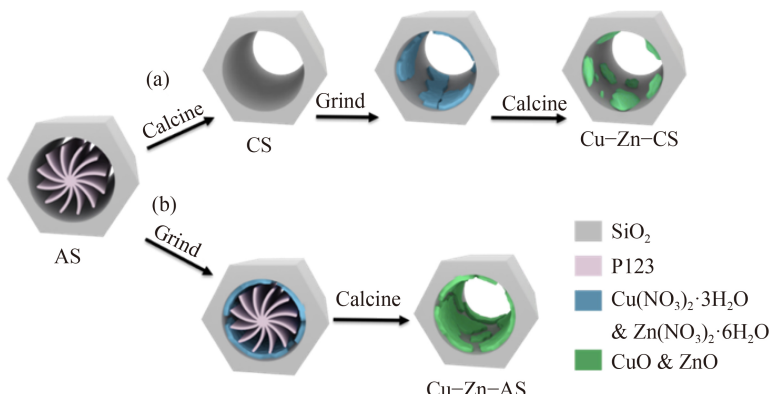


**Fig. 1** Formation of (a) aggregated CuO and ZnO via the conventional preparation process and (b) highly dispersed CuO and ZnO by using the confined space in AS.

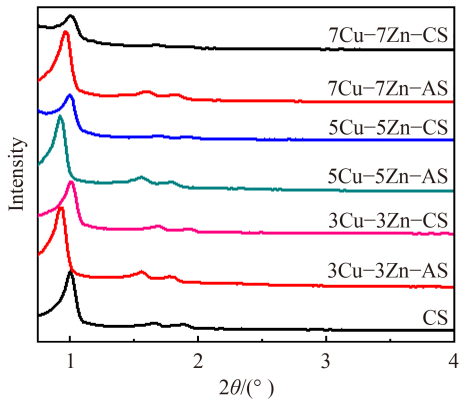


**Fig. 2** Low-angle XRD patterns of CS, Cu–Zn–AS, and Cu–Zn–CS.

unit cell constant was calculated to be 10.9 nm, which is higher than that of the CS samples (10.2 nm). This result indicates that the presence of Cu and Zn guests prevents the shrinkage of the framework during calcination.

All samples present a broad diffraction peak centered at 23° in the wide-angle XRD patterns (Fig. 3); this peak corresponds to the amorphous silica walls. 3Cu–3Zn–AS and 5Cu–5Zn–AS are similar to the carrier. 7Cu–7Zn–AS, however, shows some diffraction peaks at the  $2\theta$  values of 36° and 39°, which are attributed to CuO, and those at 31°, 34° and 36° are attributed to ZnO. This finding demonstrates that when the content of CuO and ZnO was increased to 7 mmol·g<sup>-1</sup>, the active components were not well-dispersed throughout the pores. The 3Cu–3Zn–CS derived from the CS shows strong characteristic diffraction peaks attributed to CuO. With increasing loading, all Cu–Zn–CS samples display much stronger diffraction peaks than their Cu–Zn–AS analogs. Based on the above analysis, it is reasonable to conclude

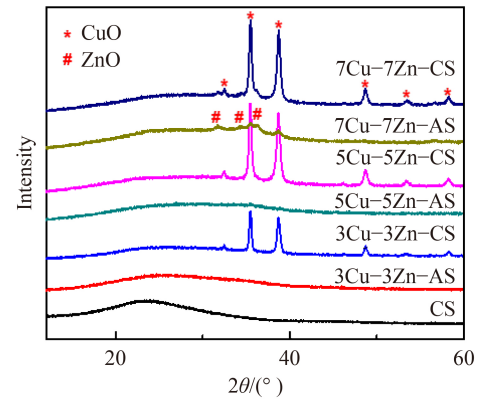


**Fig. 3** Wide-angle XRD patterns of CS, Cu–Zn–AS, and Cu–Zn–CS.

that the use of the confined space in the AS can promote the dispersion of bimetallic active components.

$N_2$  adsorption and desorption isotherms provide other important information. As shown in Fig. 4, all samples display a type IV isotherm with an H1 hysteresis loop, which indicates that all samples retain their regular mesoporous structure. Compared to the AS-derived samples, the CS-derived samples show a tail at the desorption stage, which is more obvious with the increase in Cu and Zn loading. In addition, the hysteresis loop decreases when the loading is increased. The pore size distributions show that all the AS-derived samples have a pore size similar to that of the carrier, and this pore size is higher than that of the CS-derived samples. In addition, the specific surface areas of the AS-derived samples are larger than their counterparts derived from CS (Table 1). Based on the above results, it is reasonable to conclude that the active components in the Cu–Zn–CS aggregate and the active components in Cu–Zn–AS are more

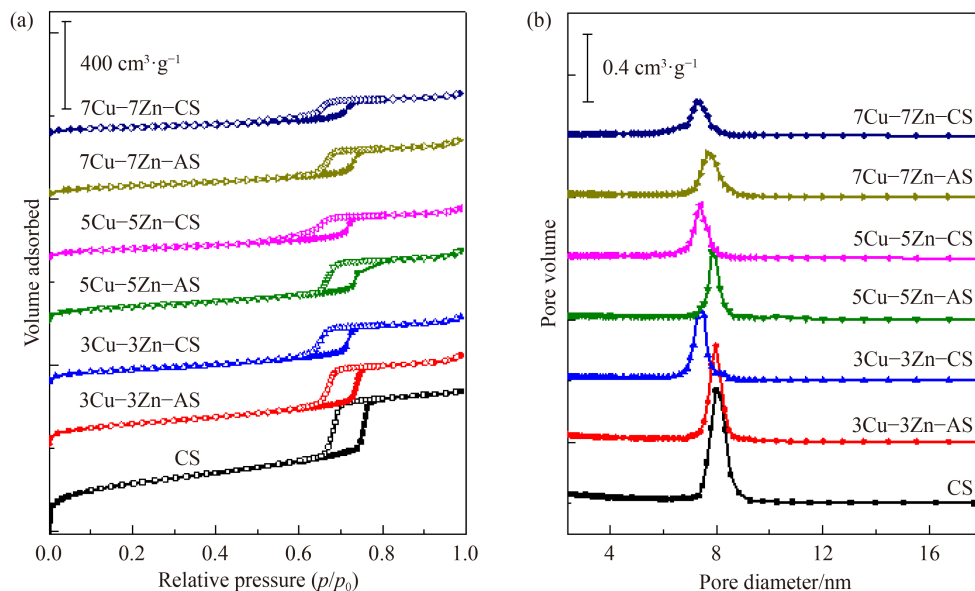


**Fig. 4** (a)  $N_2$  adsorption–desorption isotherms and the corresponding (b) pore size distributions of CS, Cu–Zn–AS, and Cu–Zn–CS (Curves were plotted offset for clarity).

**Table 1** Textual parameters of the samples CS, Cu-Zn-AS, and Cu-Zn-CS

Sample	$S_{\text{BET}}/(\text{m}^2 \cdot \text{g}^{-1})^{\text{a)}$	$V_p/(\text{cm}^3 \cdot \text{g}^{-1})$	$D_p/\text{nm}$
CS	814	0.938	8.14
3Cu-3Zn-AS	429	0.707	7.98
5Cu-5Zn-AS	303	0.540	7.82
7Cu-7Zn-AS	233	0.440	7.68
3Cu-3Zn-CS	290	0.520	7.44
5Cu-5Zn-CS	221	0.397	7.40
7Cu-7Zn-CS	168	0.323	7.26

a)  $S_{\text{BET}}$ , total specific surface area from Brunner–Emmett–Teller (BET) method.

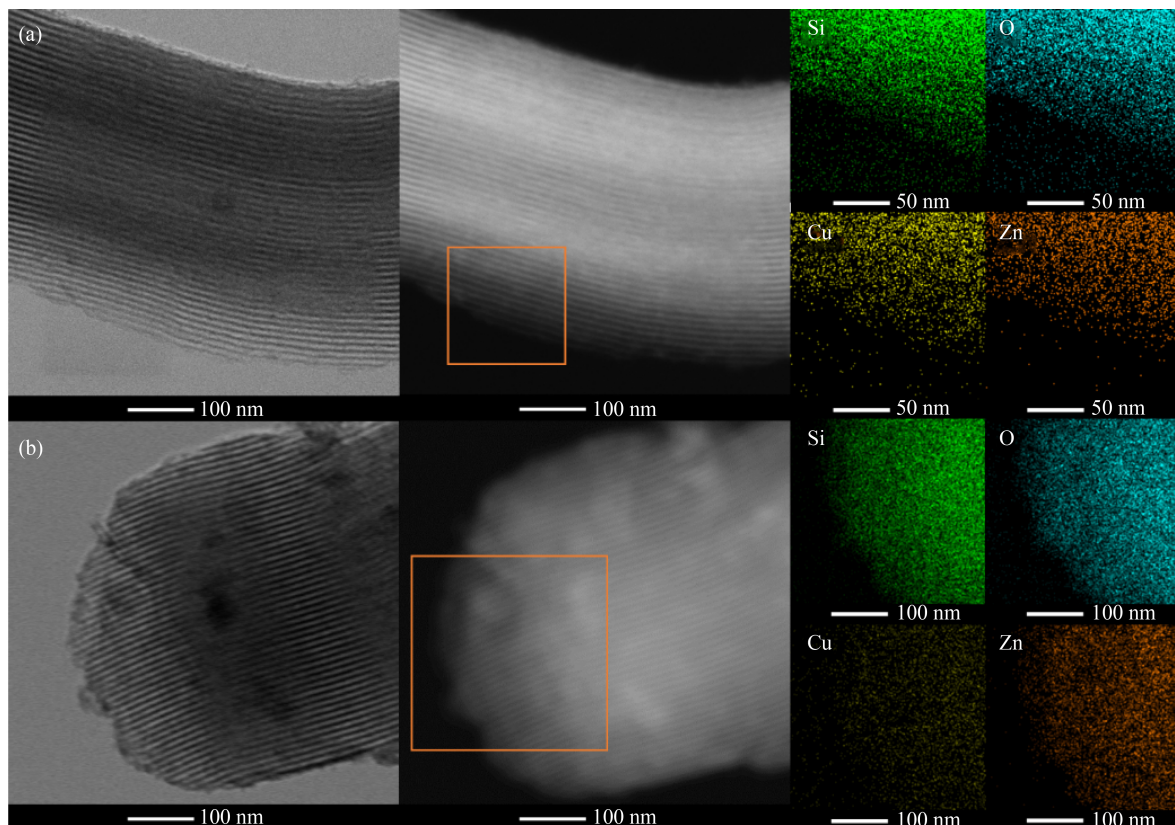
highly dispersed.

Figure 5 shows typical transmission electron microscope (TEM) images of the Cu-Zn-AS and Cu-Zn-CS. An ordered mesoporous structure can be seen in the images. This result reflects that after Cu and Zn are loaded, the structure of the carrier is not destroyed. Moreover, no aggregated particles can be seen in the TEM image of the 3Cu-3Zn-AS, which indicates that Cu and Zn are highly dispersed. The elemental mapping image of the 3Cu-3Zn-AS also shows that Cu and Zn are evenly distributed. Conversely, aggregation of CuO and ZnO can be observed in the TEM image of the 3Cu-3Zn-CS; this finding is consistent with the previous XRD results. Hence, it is obvious that the samples prepared using confined space have better dispersion.

In short, based on the XRD, N<sub>2</sub> adsorption, and TEM results, the AS-derived samples have better-dispersed active components than the CS-derived samples. This finding suggests that the confined space between the template and silica walls can promote the dispersion of active components.

### 3.2 Proposed mechanism for dispersion

Based on the abovementioned results, it is apparent that CuO and ZnO can be well dispersed by using the confined space in the AS. To explore the dispersion mechanism, the samples were examined by thermal gravity (TG) before calcination, and the results are shown in Fig. 6. The decomposition of template P123 in AS occurred at approximately 190 °C, which is a lower decomposition temperature than that of pure P123 (210 °C). The reason for the low temperature is that silica walls can catalyze the decomposition of the template. However, the decomposition temperature of P123 in the 3Cu-3Zn-AS sample is 250 °C, which is obviously higher than that of pure P123. Other samples also show a similar trend (Figs. S1 and S2, cf. Electronic Supplementary Material, ESM). This result indicates that the Cu and Zn precursors were successfully introduced into the confined space of the AS, and they separated the P123 template from the silica walls and hindered the



**Fig. 5** Bright-field and dark-field TEM images as well as elemental mapping of the samples (a) 3Cu-3Zn-AS and (b) 3Cu-3Zn-CS.

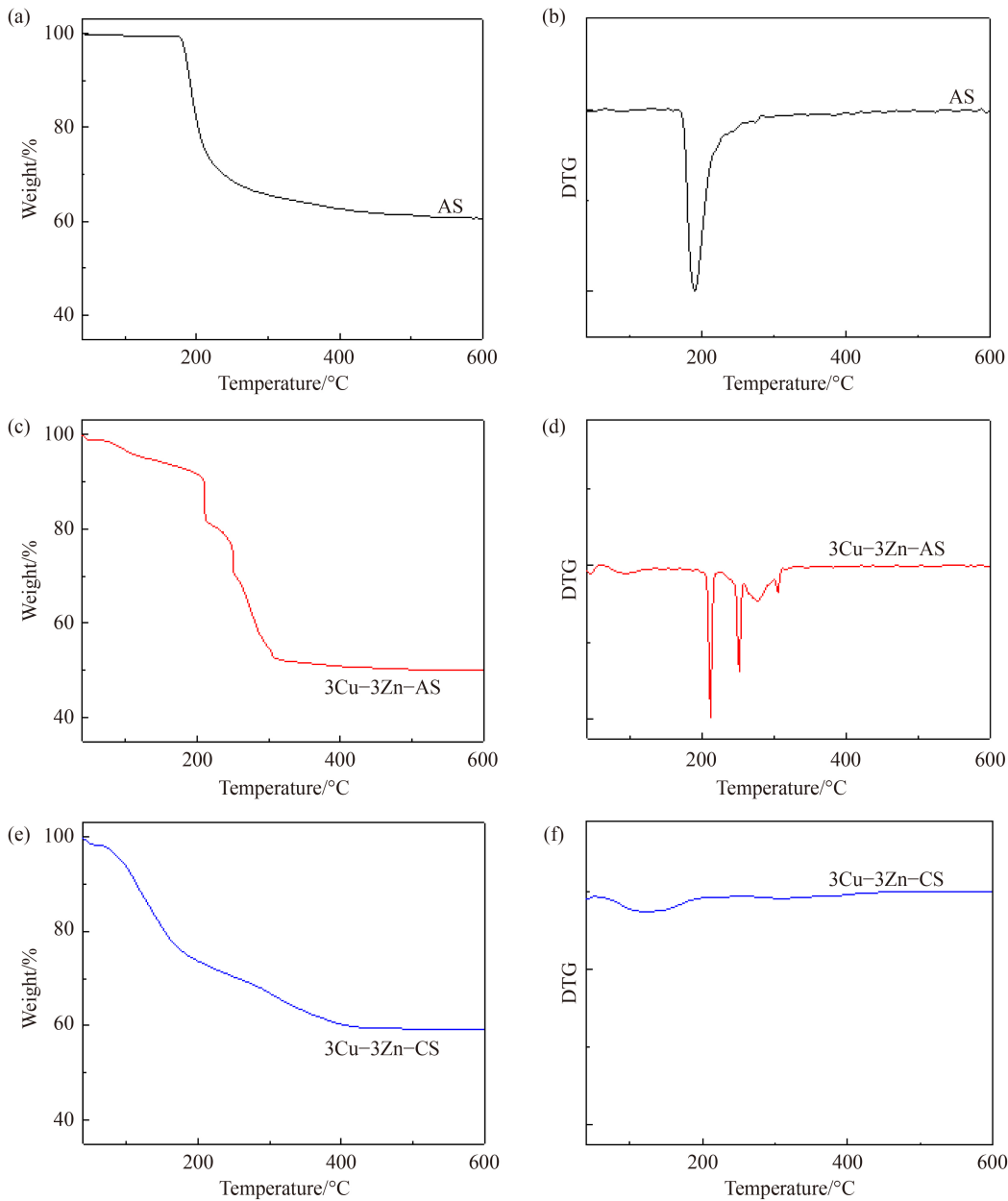


**Fig. 6** (a, c, e) TG and (b, d, f) DTG curves of Cu–Zn–AS and Cu–Zn–CS before calcination.

catalysis of the silica walls and the decomposition of P123. For the CS-derived samples, two derivative thermogravimetry (DTG) peaks are present at 180 and 280 °C; these peaks appear due to the conversion of Zn and Cu precursors to their respective oxides. The presence of confined space in the AS was also explored by measuring the N<sub>2</sub> adsorption. Some nitrogen can adsorb onto the AS, and the pore size distribution was observed (Fig. S3, cf. ESM). After the introduction of the Cu and Zn precursors, the adsorption amount decreased obviously, and the pore size distributions become invisible. This result reflects the introduction of precursors to the confined space.

In addition, the abundant Si–OH groups in the AS favor

the dispersion of active components. The samples were monitored by IR before and after calcination, and the results are shown in Fig. 7. The bands located at 285–3000 and 1350–1500 cm<sup>-1</sup>, which are caused by C–H stretching and bending vibrations, can be attributed to P123. The band at 960 cm<sup>-1</sup> originates from the stretching vibration of Si–OH. After calcination, the relative intensity of the peak corresponding to Si–OH in the carrier decreases, and the vibration peak corresponding to the C–H bond in template P123 disappears due to the decomposition of P123. In addition, when the Cu and Zn precursors were introduced to the carrier AS, the antisymmetric stretching vibration of the N–O bond appeared at 1380 cm<sup>-1</sup> and disappeared after

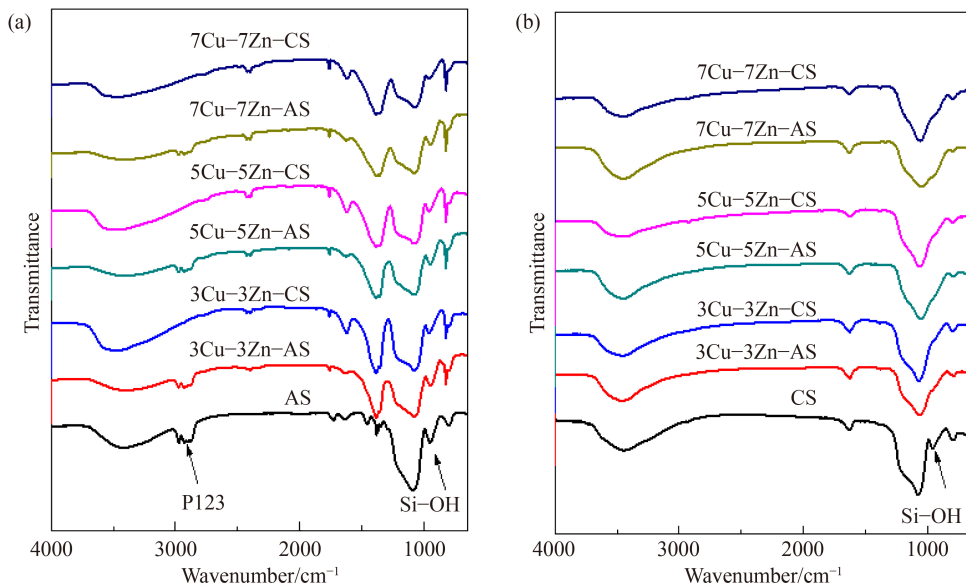


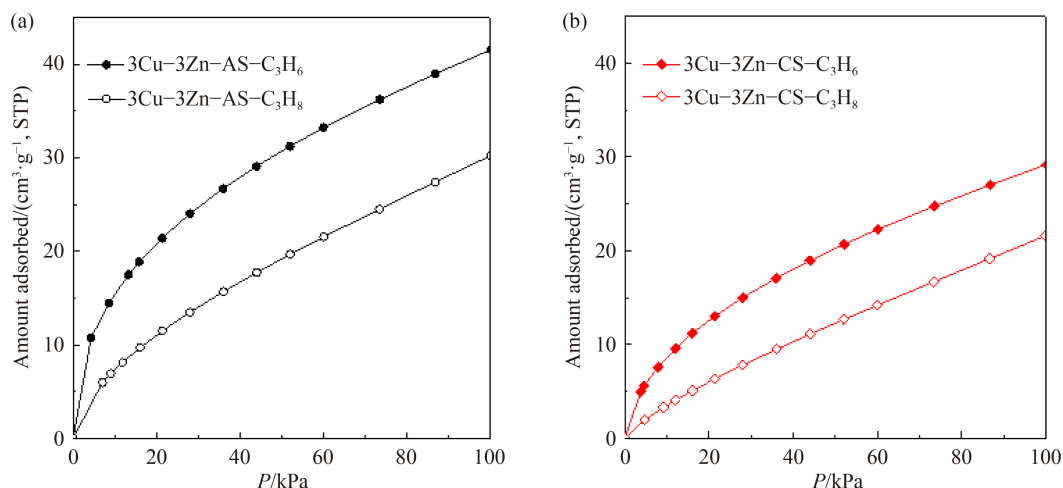
**Fig. 7** Infrared spectra of Cu-Zn-AS and Cu-Zn-CS (a) before and (b) after calcination.

calcination. This result suggests that calcination leads not only to the decomposition of the template in the channel but also to the conversion of the nitrate precursors. Based on the above analysis, the confined space and strong interactions caused by the abundant hydroxyl groups are responsible for the good dispersion of CuO and ZnO.

### 3.3 Adsorption performance of the resultant materials

$C_3H_6$  is one of the most important chemical raw materials, and the separation of  $C_3H_6$  and  $C_3H_8$  is key for its production. Because their molecular size is similar and the difference in their volatilities is small, their separation by distillation is quite energy intensive. Much attention has been given to the separation of  $C_3H_6$  from  $C_3H_8$  by using adsorption. The resultant Cu-Zn bimetallic adsorbents were employed in the separation of  $C_3H_6$  from  $C_3H_8$ , and the results are shown in Fig. 8. The sample 3Cu-

3Zn-AS adsorbed  $41.5 \text{ cm}^3 \cdot \text{g}^{-1}$   $C_3H_6$  and  $30.2 \text{ cm}^3 \cdot \text{g}^{-1}$   $C_3H_8$  under 100 kPa, while under the same conditions, the sample 3Cu-3Zn-CS only adsorbed  $39.2 \text{ cm}^3 \cdot \text{g}^{-1}$   $C_3H_6$  and  $21.6 \text{ cm}^3 \cdot \text{g}^{-1}$   $C_3H_8$ . In addition, as the loading of Cu and Zn was increased, the adsorption of  $C_3H_6$  and  $C_3H_8$  on the AS-derived sample surpassed that of the CS-derived analogs. To further study the adsorption behavior of Cu-Zn bimetallic adsorbents, we estimated the adsorption selectivity of the Cu-Zn bimetallic adsorbents based on the ideal adsorbed solution theory, as shown in Fig. 9. All AS-derived samples were more selective than CS-derived samples. In particular, when the  $C_3H_6$  molar fraction was 0.1, the selectivity for  $C_3H_6$  over  $C_3H_8$  on 5Cu-5Zn-AS was 3.5, which is obviously higher than that on 5Cu-5Zn-CS (2.4). These results thus demonstrate that the AS-derived samples, which had better-dispersed active components, exhibited better adsorption performance.



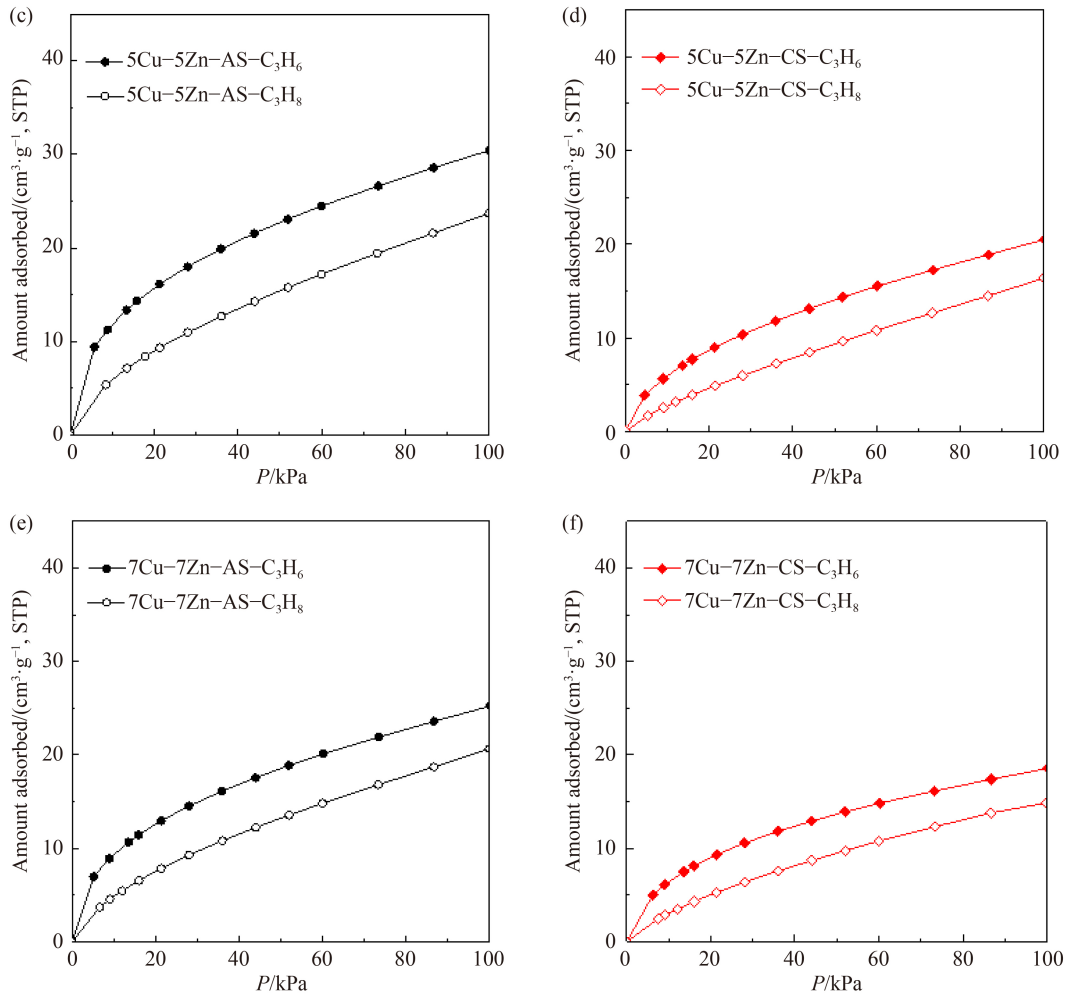


**Fig. 8** Adsorption isotherms of  $\text{C}_3\text{H}_6$  and  $\text{C}_3\text{H}_8$  over the samples (a, c, e) Cu–Zn–AS and (b, d, f) Cu–Zn–CS.

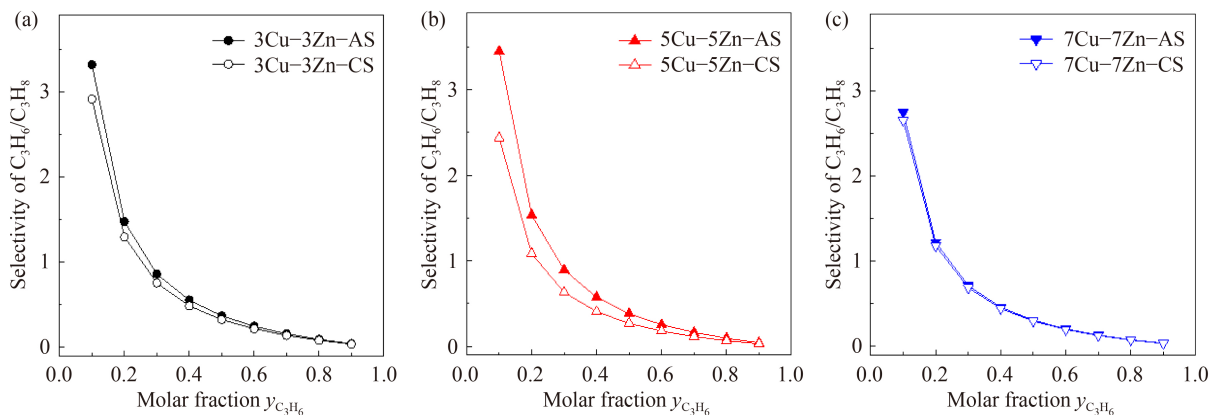


**Fig. 9** Selectivity of  $\text{C}_3\text{H}_6$  over  $\text{C}_3\text{H}_8$  on the samples (a) 3Cu–3Zn–AS and 3Cu–3Zn–CS, (b) 5Cu–5Zn–AS and 5Cu–5Zn–CS, and (c) 7Cu–7Zn–AS and 7Cu–7Zn–CS.

## 4 Conclusions

A simple but efficient strategy has been designed to disperse CuO and ZnO by utilizing the confined space

between silica walls and the template in unmodified mesoporous silica. Up to 5 mmol·g<sup>-1</sup> of CuO and ZnO can be well dispersed in SBA-15, whereas noticeable aggregation takes place in the counterpart prepared from the conventional support, which does not contain

confined spaces. The plentiful hydroxyl groups on the surface also play a necessary role. The resultant bimetallic adsorbents derived from the AS exhibit better performance in the selective adsorption of  $C_3H_6$  over  $C_3H_8$  in comparison with their counterparts from the CS. The present strategy may enable us to fabricate functional materials decorated with various active components with high dispersion for different applications.

**Acknowledgements** We acknowledge the financial support of this work by the National Natural Science Foundation of China (Grant Nos. 22125804, 22078155, and 21878149).

**Electronic Supplementary Material** Supplementary material is available in the online version of this article at <https://dx.doi.org/10.1007/s11705-022-2202-y> and is accessible for authorized users.

## References

- Nugent P, Belmabkhout Y, Burd S D, Cairns A J, Luebke R, Forrest K, Pham T, Ma S, Space B, Wojtas L, Eddaudi M, Zaworotko M J. Porous materials with optimal adsorption thermodynamics and kinetics for  $CO_2$  separation. *Nature*, 2013, 495(7439): 80–84
- Liu M, Zhang L, Little M A, Kapil V, Ceriotti M, Yang S, Ding L, Holden D L, Balderas-Xicohténcatl R, He D, Clowes R, Chong S Y, Schütz G, Chen L, Hirscher M, Cooper A I. Barely porous organic cages for hydrogen isotope separation. *Science*, 2019, 366(6465): 613–620
- Sholl D S, Lively R P. Seven chemical separations to change the world. *Nature*, 2016, 532(7600): 435–437
- Karmakar A, Desai A V, Manna B, Joarder B, Ghosh S K. An amide-functionalized dynamic metal-organic framework exhibiting visual colorimetric anion exchange and selective uptake of benzene over cyclohexane. *Chemistry*, 2015, 21(19): 7071–7076
- Zhang K, Lively R P, Dose M E, Brown A J, Zhang C, Chung J, Nair S, Koros W J, Chance R R. Alcohol and water adsorption in zeolitic imidazolate frameworks. *Chemical Communications*, 2013, 49(31): 3245–3247
- Bhadra B N, Vinu A, Serre C, Jhung S H. MOF-derived carbonaceous materials enriched with nitrogen: preparation and applications in adsorption and catalysis. *Materials Today*, 2019, 25: 88–111
- Bui T X, Choi H. Adsorptive removal of selected pharmaceuticals by mesoporous silica SBA-15. *Journal of Hazardous Materials*, 2009, 168(2–3): 602–608
- Li P Z, Wang X J, Tan S Y, Ang C Y, Chen H, Liu J, Zou R, Zhao Y. Clicked isoreticular metal-organic frameworks and their high performance in the selective capture and separation of large organic molecules. *Angewandte Chemie International Edition*, 2015, 54(43): 12748–12752
- Shi S, Li Y X, Li S S, Liu X Q, Sun L B. Fabrication of  $Cu^+$  sites in confined spaces for adsorptive desulfurization by series connection double-solvent strategy. *Green Energy & Environment*, 2022, 7(2): 345–351
- Gu C, Weng W, Lu C, Tan P, Jiang Y, Zhang Q, Liu X, Sun L. Decorating MXene with tiny ZIF-8 nanoparticles: an effective approach to construct composites for water pollutant removal. *Chinese Journal of Chemical Engineering*, 2022, 42: 42–48
- Ma S, Zhou H C. Gas storage in porous metal-organic frameworks for clean energy applications. *Chemical Communications*, 2010, 46(1): 44–53
- Tan P, Jiang Y, Wu Q, Gu C, Qi S, Zhang Q, Liu X, Sun L. Light-responsive adsorbents with tunable adsorbent-adsorbate interactions for selective  $CO_2$  capture. *Chinese Journal of Chemical Engineering*, 2022, 42: 104–111
- Tan P, Jiang Y, Qi S C, Gao X J, Liu X Q, Sun L B. Ce-doped smart adsorbents with photoresponsive molecular switches for selective adsorption and efficient desorption. *Engineering (Beijing)*, 2020, 6(5): 569–576
- Zhao X, Yuan Y, Li P, Song Z, Ma C, Pan D, Wu S, Ding T, Guo Z, Wang N. A polyether amine modified metal organic framework enhanced the  $CO_2$  adsorption capacity of room temperature porous liquids. *Chemical Communications (Cambridge)*, 2019, 55(87): 13179–13182
- Alsbæe A, Smith B J, Xiao L, Ling Y, Helbling D E, Dichtel W R. Rapid removal of organic micropollutants from water by a porous  $\beta$ -cyclodextrin polymer. *Nature*, 2016, 529(7585): 190–194
- Zhang T, Huang X, Asefa T. Nanostructured polymers with high surface area using inorganic templates for the efficient extraction of anionic dyes from solutions. *Chemical Communications*, 2015, 51(89): 16135–16138
- Yoo D K, Yoon T U, Bae Y S, Jhung S H. Metal-organic framework MIL-101 loaded with polymethacrylamide with or without further reduction: effective and selective  $CO_2$  adsorption with amino or amide functionality. *Chemical Engineering Journal*, 2020, 380: 122496
- Qi S C, Xue D M, Yu G X, Zhu R R, Liu X Q, Sun L B. An antiempirical strategy: sacrificing aromatic moieties in the polymer precursor for improving the properties of the derived N-doped porous carbons. *Green Chemical Engineering*, 2020, 1(1): 70–76
- Yoo C J, Narayanan P, Jones C W. Self-supported branched poly(ethyleneimine) materials for  $CO_2$  adsorption from simulated flue gas. *Journal of Materials Chemistry A: Materials for Energy and Sustainability*, 2019, 7(33): 19513–19521
- Siegelman R L, Milner P J, Kim E J, Weston S C, Long J R. Challenges and opportunities for adsorption-based  $CO_2$  capture from natural gas combined cycle emissions. *Energy & Environmental Science*, 2019, 12(7): 2161–2173
- Pardakhti M, Jafari T, Tobin Z, Dutta B, Moharreri E, Shemshaki N S, Suib S, Srivastava R. Trends in solid adsorbent materials development for  $CO_2$  capture. *ACS Applied Materials & Interfaces*, 2019, 11(38): 34533–34559
- Subhan F, Aslam S, Yan Z, Zhen L, Ikram M, Ullah R, Etim U J, Ahmad A. Ammonia assisted functionalization of cuprous oxide within confined spaces of SBA-15 for adsorptive desulfurization. *Chemical Engineering Journal*, 2018, 339: 557–565
- Alkhabbaz M A, Bollini P, Foo G S, Sievers C, Jones C W. Important roles of enthalpic and entropic contributions to  $CO_2$

- capture from simulated flue gas and ambient air using mesoporous silica grafted amines. *Journal of the American Chemical Society*, 2014, 136(38): 13170–13173
24. Kou J, Lu C, Sun W, Zhang L, Xu Z. Facile fabrication of cuprous oxide-based adsorbents for deep desulfurization. *ACS Sustainable Chemistry & Engineering*, 2015, 3(12): 3053–3061
  25. Kuwahara Y, Kang D Y, Copeland J R, Brunelli N A, Didas S A, Bollini P, Sievers C, Kamegawa T, Yamashita H, Jones C W. Dramatic enhancement of CO<sub>2</sub> uptake by poly(ethyleneimine) using zirconosilicate supports. *Journal of the American Chemical Society*, 2012, 134(26): 10757–10760
  26. Giret S, Wong Chi Man M, Carcel C. Mesoporous-silica-functionalized nanoparticles for drug delivery. *Chemistry*, 2015, 21(40): 13850–13865
  27. Zhang X, Qu Z, Yu F, Wang Y. High-temperature diffusion induced high activity of SBA-15 supported Ag particles for low temperature CO oxidation at room temperature. *Journal of Catalysis*, 2013, 297(0): 264–271
  28. Wang P, Zheng X, Wu X, Wei X, Zhou L. Preparation and characterization of CuO nanoparticles encapsulated in mesoporous silica. *Microporous and Mesoporous Materials*, 2012, 149(1): 181–185
  29. Wu Z, Zhao D. Ordered mesoporous materials as adsorbents. *Chemical Communications*, 2011, 47(12): 3332
  30. Zhao D Y, Huo Q S, Feng J L, Chmelka B F, Stucky G D. Nonionic triblock and star diblock copolymer and oligomeric surfactant syntheses of highly ordered, hydrothermally stable, mesoporous silica structures. *Journal of the American Chemical Society*, 1998, 120(24): 6024–6036
  31. Zhao D Y, Feng J L, Huo Q S, Melosh N, Fredrickson G H, Chmelka B F, Stucky G D. Triblock copolymer syntheses of mesoporous silica with periodic 50 to 300 angstrom pores. *Science*, 1998, 279(5350): 548–552
  32. Zhang Z, Melián-Cabrera I. Modifying the hierarchical porosity of SBA-15 via mild-detemplation followed by secondary treatments. *Journal of Physical Chemistry C*, 2014, 118(49): 28689–28698
  33. Zheng Q, Zhu Y, Xu J, Cheng Z, Li H, Li X. Fluoroalcohol and fluorinated-phenol derivatives functionalized mesoporous SBA-15 hybrids: high-performance gas sensing toward nerve agent. *Journal of Materials Chemistry*, 2012, 22(5): 2263–2270
  34. Zhi J, Song D, Li Z, Lei X, Hu A. Palladium nanoparticles in carbon thin film-lined SBA-15 nanoreactors: efficient heterogeneous catalysts for Suzuki-Miyaura cross coupling reaction in aqueous media. *Chemical Communications*, 2011, 47(38): 10707–10709
  35. Wu Z, Zhu W, Zhang M, Lin Y, Xu N, Chen F, Wang D, Chen Z. Adsorption and synergistic fenton-like degradation of methylene blue by a novel mesoporous  $\alpha$ -Fe<sub>2</sub>O<sub>3</sub>/SiO<sub>2</sub> at neutral pH. *Industrial & Engineering Chemistry Research*, 2018, 57(16): 5539–5549
  36. Wu Z, Lu Q, Fu W H, Wang S, Liu C, Xu N, Wang D, Wang Y M, Chen Z. Fabrication of mesoporous Al-SBA-15 as a methylene blue capturer via a spontaneous infiltration route. *New Journal of Chemistry*, 2015, 39(2): 985–993
  37. Wang Y M, Wu Z Y, Wang H J, Zhu J H. Fabrication of metal oxides occluded in ordered mesoporous hosts via a solid-state grinding route: the influence of host-guest interactions. *Advanced Functional Materials*, 2006, 16(18): 2374–2386
  38. Yin Y, Jiang W J, Liu X Q, Li Y H, Sun L B. Dispersion of copper species in a confined space and their application in thiophene capture. *Journal of Materials Chemistry*, 2012, 22(35): 18514
  39. Shi L Y, Li Y X, Xue D M, Tan P, Jiang Y, Liu X Q, Sun L B. Fabrication of highly dispersed nickel in nanoconfined spaces of as-made SBA-15 for dry reforming of methane with carbon dioxide. *Chemical Engineering Journal*, 2020, 390: 124491
  40. Wang T, Li X, Dai W, Fang Y, Huang H. Enhanced adsorption of dibenzothiophene with zinc/copper-based metal-organic frameworks. *Journal of Materials Chemistry A: Materials for Energy and Sustainability*, 2015, 3(42): 21044–21050
  41. Khan N A, Kim C M, Jhung S H. Adsorptive desulfurization using Cu-Ce/metal-organic framework: improved performance based on synergy between Cu and Ce. *Chemical Engineering Journal*, 2017, 311: 20–27
  42. Danmaliki G I, Saleh T A. Effects of bimetallic Ce/Fe nanoparticles on the desulfurization of thiophenes using activated carbon. *Chemical Engineering Journal*, 2017, 307: 914–927
  43. Kou Y, Sun L B. Size regulation of platinum nanoparticles by using confined spaces for the low-temperature oxidation of ethylene. *Inorganic Chemistry*, 2018, 57(3): 1645–1650
  44. Gu M X, Kou Y, Qi S C, Shao M Q, Yue M B, Liu X Q, Sun L B. Highly dispersive cobalt oxide constructed in confined space for oxygen evolution reaction. *ACS Sustainable Chemistry & Engineering*, 2019, 7(2): 2837–2843
  45. Kong L, Zhang T, Yao R, Zeng Y, Zhang L, Jian P. Adsorptive desulfurization of fuels with Cu(I)/SBA-15 via low-temperature reduction. *Microporous and Mesoporous Materials*, 2017, 251: 69–76